



Coupled effect of water absorption and ion transport in hydrated latex anti-corrosion coatings

Yu Ren Zhou , Surya Effendy, Juner Zhu, Michael T. Petr, Colin D. Cwalina, Martin Z. Bazant, Bilge Yildiz, Ju Li, Michael P. Short

Received: 18 January 2022 / Revised: 20 May 2022 / Accepted: 12 June 2022
© The Author(s) 2022

Abstract Water-based anti-corrosion coatings, which are environmentally-friendly replacements for organic solvent-based coatings, do not perform well enough for use in the most challenging corrosion environments. The high water absorption capacity of water-based latex films may reduce barrier performance by contributing to corrosive reactant/product transport. We seek to understand the coupled effects of water absorption and ion transport in hydrated latex films, and to propose mechanisms explaining these effects. Water absorption and ion transport in films immersed in deionized (DI) water were monitored by mass gain

and electrical conductivity measurements, respectively. Despite very similar polymer compositions between films, large differences in water absorption and ion transport rates were observed and explained by percolating networks at latex particle boundaries which facilitate transport. A semi-continuum model with three-component diffusion and convection-like elastic relaxation supported the assumptions of the physical mechanisms governing water absorption and ion transport. The evidence of the coupled processes of water absorption and ion transport in hydrated latex films revealed in this study are useful for designing water-based coatings that provide high levels of corrosion resistance.

Supplementary Information The online version contains supplementary material available at <https://doi.org/10.1007/s11998-022-00676-0>.

Keywords Water absorption, Ion transport, Swelling, Latex film, Modelling

Y. R. Zhou (✉), B. Yildiz, J. Li
Department of Materials Science and Engineering,
Massachusetts Institute of Technology, Cambridge, MA
02139, USA
e-mail: wyrzhou@mit.edu

S. Effendy, J. Zhu, M. Z. Bazant
Department of Chemical Engineering, Massachusetts
Institute of Technology, Cambridge, MA 02139, USA

J. Zhu
Department of Mechanical Engineering, Massachusetts
Institute of Technology, Cambridge, MA 02139, USA

M. T. Petr, C. D. Cwalina
Dow Inc., 400 Arcola Road, Collegeville, PA 19426, USA

M. Z. Bazant
Department of Mathematics, Massachusetts Institute of
Technology, Cambridge, MA 02139, USA

B. Yildiz, J. Li, M. P. Short
Department of Nuclear Science and Engineering,
Massachusetts Institute of Technology, Cambridge, MA
02139, USA

Introduction

Coatings are a cost-effective, easily-applied and scalable method of protecting metal surfaces, such as carbon steel, against corrosion. Paint, composed of polymers and other additives dissolved or dispersed in a suitable carrier, is applied to a surface with a wet thickness on the order of 100 μm . The solid film, which forms after evaporation of volatile components, functions as a physical barrier against corrosive reactants, such as water, oxygen, and salts. Much work has focused on the development of water-based anti-corrosion coatings, in which components are initially dispersed or dissolved in water, to reduce the environmental damage caused by the use of solvent-based coatings, which release organic vapor during solvent evaporation.¹ Polymers can be dispersed as latex colloids in water-based paint synthesized by emulsion polymerization as in this study. Film formation from a latex dispersion consists of three stages, as categorized

by Steward et al.² First, water evaporation raises the latex solids' volume fraction until particles come into close contact and occupy a total volume fraction of 60–70%. Second, packed particles deform to fill interparticle voids in the film. Third, polymer chains interdiffuse across latex particle boundaries, promoting chemical and free-volume homogeneities and reducing the distinction between individual particles. The dried films of practical latex coatings for corrosion protection typically consist of inorganic pigment particles such as titanium dioxide (TiO₂) dispersed inside an organic matrix, which consists mostly of polymer along with residual coalescent, surfactant, dispersant, and other minor components.

Because they have some hydrophilicity, latex films often absorb an extraordinary amount of water, sometimes in excess of 100% of their dry mass.^{3–8} The effect of film composition on water absorption has been studied extensively. Indeed, raising film hydrophobicity by increasing the concentration of fluorinated monomers^{9–16} has been shown effective in reducing water absorption, but fluorinated latexes are limited by high financial cost^{10,11,13} and difficulty in synthesis due to chemical incompatibility between fluorinated molecules and water.^{12,15} Raising film hydrophilicity has the opposite effect, as increasing concentration of polar functional groups, such as carboxylic acid,^{8,17} hydroxyl^{8,18–20} and sulfonic acid,²¹ raises water absorption. Another important aspect, polymer mechanical properties also influence water absorption. Crosslinking between polymer chains^{7,8,22} and higher glass transition temperature (T_g)^{20,23,24} both reduce water absorption. Finally, both covalently and non-covalently bound emulsifiers have a significant effect on water absorption, as increasing emulsifier concentration raises water absorption.^{10, 16, 25–27} Previous studies showed that ion transport in hydrogels is strongly affected by the amount of absorbed water.^{28,29} When the absorbed water volume fraction in a polyethylene oxide hydrogel was raised from 29 to 81 vol.%, NaCl permeability increased by a factor of 140.²⁸ Faster ion transport may lead to higher corrosion rates of a metal substrate, as higher chloride anion concentration leads to exacerbated pitting corrosion in stainless steel³⁰ and accelerated corrosion of carbon steel.³¹ Therefore, absorbed water in latex films may have a significant effect on ion transport rate and, hence, anti-corrosion effectiveness of these films. However, ion transport in latex films, and its relationship to water absorption, has not been well studied. Dillon et al. observed ion transport kinetics by measuring electrical conductance and capacitance of a latex film under cyclic applied pressure exposed to different concentrations of Na⁺(aq) on each side, in addition to tracking the lower concentration side's Na⁺(aq) concentration using an ion-selective electrode.³² This study concluded that film mechanical failure under pressure cycling occurred by (1) formation of thin spots with negligible ion permeation, followed by (2) formation of pores leading to significant ion permeation, followed by (3) catastrophic

failure. An et al. measured ion equilibrium absorption and diffusivity in latex films with aqueous solutions of different ion concentrations on each side by tracking masses of ions transported through films versus time using electrical conductivity or ion chromatography.³³ Ions with larger diameters were found to have lower diffusivity in latex films, while potassium salts showed higher solubility in latex films compared to ammonium salts with the same anion. However, neither study examined a possible correlation between ion transport and water absorption.

To that end, this study investigates the mutual influences of water absorption and ion transport in hydrated latex films using model systems of acrylic latex and TiO₂ filler particles. Schematic representations of water absorption into, and ion transport out of, hydrated latex films measured in this study are shown in Fig. 1. Through comparison between water absorption and ion transport measurements supplemented by structural characterization, it was found that (1) absorbed water enhanced ion diffusivity, and (2) both water absorption and ion transport were accelerated by a more hydrophilic percolating latex particle boundary network. It is assumed that the behavior of the ions investigated in this study can be generalized to more corrosive ions such as chloride.

Methodology

Paint composition

Model water-based paints were provided by Dow. Paints with 35 vol.% solids contained acrylic latex particles with one of two surface chemistries—control or a Dow-proprietary surface-functionalization (SF)—but with very similar bulk polymer chemistry and were either non-pigmented (NP) or contained 200 nm-diameter rutile TiO₂ particles with 16 vol.% concentration after film formation. Typical procedures for the preparation of the paint are given in US patent 6756459 B2. The glass transition temperature (T_g) of latex particles after emulsion polymerization, but with no further additives, ranges from –20 to 60°C, with the

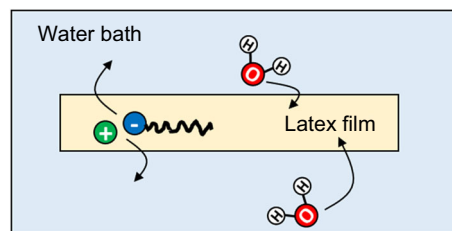


Fig. 1: A schematic representation of water absorption and ion transport in hydrated latex films which are measured in this study. Transport of the types of ionic surfactants used for emulsion polymerization³⁴ within formed latex films near room temperature has been observed in previous studies^{35, 36}

exact value depending on the monomer composition and experimental procedure. However, since control and SF latex particles were prepared according to very similar recipes, these two types of particles should have very similar values of T_g . Coalescent was added to the paint following emulsion polymerization synthesis of the latex particles at a typical level of 6 wt.%.

Water absorption

Control-NP, SF-NP, control-TiO₂, and SF-TiO₂ paints were applied onto non-stick RP-1K release papers (Leneta) using steel drawdown bars (BYK-Gardner, Gardco), film formation occurred at 25°C and 30–40% average relative humidity for 24 h, then free-standing films were carefully peeled from release papers. Water absorption measurements were performed on 5 free-standing samples of each film composition, with 24–35 cm² area per sample, to minimize random error. The thicknesses of all samples were measured to be 44–64 μm using a CG206 coating thickness gauge (Extech). The average thickness of all samples of each film composition ranged from 50 to 61 μm. Each sample was weighed after film formation using an electronic balance (VWR), then immediately immersed in 250 mL deionized (DI) water in a glass jar. Subsequent weighing occurred every 2 h between 0 and 12 h after immersion, every 12 h between 12 and 324 h after immersion, and every 24 h between 324 and 1000 h after immersion. During subsequent weighing, each sample was removed from its jar, dried with Kimwipes while placed on dry cotton wipes (Texwipe), weighed using the balance, and re-immersed in its glass jar. This process lasted for approximately 1 min per sample. Samples were kept at room temperature between 18°C and 25°C while immersed in DI water. Corrections were applied for small pieces which detached from samples during weighing and handling. Small detached pieces were discarded after detachment. The mass of a small piece from sample X weighing <5 mg which detached at time t was added to the mass of sample X measured after time t . The mass fraction reduction due to a small piece from sample X weighing >5 mg which detached at time t was used to scale the mass of sample X measured after time t .

Weighing with a finer time resolution was performed for SF-NP and SF-TiO₂ film compositions. For each film composition, 3 formed film samples with the same preparation procedure as described above were weighed after film formation, and once again after 15, 30, 45, or 60 min immersion.

Leached ion transport

The same free-standing film preparation procedure as the water absorption experiments was performed using control-NP, SF-NP, control-TiO₂, and SF-TiO₂ paints. 5 free-standing samples each of control-NP, SF-NP,

and SF-TiO₂, and 4 free-standing samples of control-TiO₂, were produced with 24–35 cm² area per sample and thicknesses between 49 and 82 μm. The average thickness of each film composition ranged from 55 to 63 μm. Each sample was immersed in a glass beaker filled with 75–80 mL DI water, together with an Orion DuraProbe 4-electrode conductivity cell (Thermo Scientific) connected to an Orion Star A212 conductivity benchtop meter (Thermo Scientific). Each beaker was stirred using a stir bar and magnetic stirrer (Thermo Scientific) and capped with a rubber stopper (Grainger) to minimize water evaporation. Electrical conductivity due to leached ions was recorded every 5 min from the start of immersion until 48–144 h after immersion for control-NP, SF-NP, and SF-TiO₂, and recorded every 30 min from the start of immersion until 960 h after immersion for control-TiO₂. Because a conductivity meter could store a maximum of 2000 conductivity measurements during each experiment, the interval between subsequent control-TiO₂ conductivity measurements was longer than those for other films. Samples were maintained at temperatures between 20 and 25°C during measurements. All conductivity measurements were corrected to a reference temperature of 25°C with a temperature compensation coefficient of 2.1%/°C. Each conductivity cell was calibrated with 100 μS/cm, 1413 μS/cm, and 12.9 mS/cm conductivity standards (Thermo Scientific) prior to immersion into a beaker.

Cross-section scanning electron microscopy (SEM)

Control-TiO₂ and SF-TiO₂ paints were applied to polyimide substrates via drawdown, then formed at 25°C and 50–70% average relative humidity for 1–14 days. The formed film thickness was approximately 100 μm. Formed film-polyimide stacks were roughly cross-sectioned using a razor blade or scissors, after which the cross-section was polished with an Ar ion cross-section polisher (JEOL). Polished, formed film cross-sections were imaged in secondary electron mode using a Zeiss Merlin or Zeiss Ultra-55 SEM (Zeiss).

Structural and chemical characterization

The structures of control-NP and SF-NP free-standing formed films were characterized using a SAXSLAB small-angle X-ray scattering (SAXS) instrument which is capable of probing length scales between 0.3 and 2000 nm in transmission mode. The chemical composition of control-NP and SF-NP films were characterized using Fourier transform infrared (FTIR) spectroscopy, using an IS50R Bench FTIR spectrometer (Thermo Fisher) in attenuated total reflection (ATR) mode, which is capable of measuring infrared absorbance between 4000 and 400 cm⁻¹ frequencies. Prior to ATR-FTIR measurements, control-NP and SF-NP films were dried in a vacuum oven at 100°C for

approximately 90 min to minimize residual water in these films.

Results and discussion

SAXS and FTIR results

Results from transmission SAXS of control-NP and SF-NP films are shown in Fig. 2. Two diffraction peaks are visible in each of the diffraction patterns. Two diffraction peaks are visible in each scattering pattern, and the ratio of peak scattering vectors in each pattern suggests that the peaks are (111) and (220) peaks of a face-centered cubic (FCC) latex particle superlattice. The (111) and (220) FCC latex superlattice peaks were also observed in latex films by Konko et al. (2019). The scattering vector is $q = \frac{4\pi\sin(\theta)}{\lambda}$, where 2θ is the scattering angle and λ is the X-ray wavelength. Interplanar spacing between (hkl) planes may be obtained from the peak scattering vector according to Bragg's law,³⁷ $d_{hkl} = \frac{\lambda}{2\sin(\theta)} = \frac{2\pi}{q}$. For a cubic crystal structure such as FCC, $d_{hkl} = \frac{a}{\sqrt{h^2+k^2+l^2}}$, where a is the lattice parameter.³⁷ Assuming that there are four latex particles in each unit cell of the FCC superlattice, latex particle diameter d in the films is given by the expression $a^3 = 4\left(\frac{\pi}{6}d^3\right)$. Therefore, the latex particles should have a diameter $d = 110$ nm in control-NP films and a diameter of $d = 140$ nm in SF-NP films, so control-NP film latex particles have only 20% lower diameter compared to SF-NP film particles. Moreover, these measured particle sizes are consistent with the preferred latex particle diameter range of 50–250 nm stated in US patent 6756459 B2.

Infrared absorption spectra of control-NP and SF-NP films measured using ATR-FTIR are shown in Fig. 3. The nearly identical position and intensity of most peaks on control-NP and SF-NP are consistent

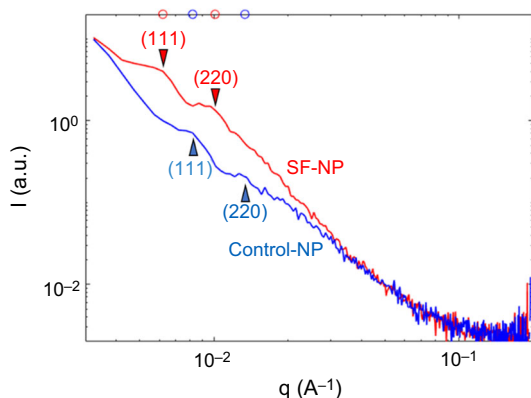


Fig. 2: Transmission SAXS results of free-standing control-NP and SF-NP films with diffracted intensity on the y-axis and scattering vector on the x-axis, showing visible (111) and (220) diffraction peaks of the FCC latex particle superlattice

with the very similar bulk latex particle composition of the films. Major peaks at frequencies greater than 1500 cm^{-1} , outside of the fingerprint region, may be identified with great confidence with the aid of an infrared absorption database. The peak at around 1700 cm^{-1} may be due C=O bond stretching, the peak at around 2200 cm^{-1} may be due to C \equiv N stretching, and the peaks between 2800 and 3100 cm^{-1} may be C–H bond stretching. The most significant difference between control-NP and SF-NP films is the more intense SF-NP peaks in the $900\text{--}1100\text{ cm}^{-1}$ frequency region, which lie in the fingerprint region and are therefore more difficult to identify. In particular, the peaks between 1000 and 1100 cm^{-1} may be due to S=O bond stretching in sulfoxide groups. Due to the very similar bulk chemistries of control and SF latex particles, the infrared absorption spectra suggest that SF surface chemistry results in a higher concentration of hydrophilic sulfoxide groups than control surface chemistry, and hence that the boundary regions between latex particles in SF latex films are more hydrophilic compared to the corresponding regions in control latex films.

The claim of higher sulfoxide group concentration on SF latex surfaces is strengthened by a study by Chellappa et al. (2015), in which TiO₂ particles were dispersed in a dimethyl sulfoxide (DMSO) solvent with high colloidal stability, as a zeta potential of 27 mV was measured for TiO₂ particles stabilized in sulfoxide group-rich DMSO. The intention of SF surface chemistry was to improve TiO₂ colloidal stability in paint, so it is possible that a sulfoxide-rich chemistry was selected by Dow when formulating the SF surface chemistry.

Water entry mechanism into latex films

Fractional mass gains of latex films during immersion in DI water as a function of time are shown in Fig. 4. A version of Fig. 4 with error bars is shown in Figure S0. The fractional mass gain is approximately proportional to the square root of time during initial water absorption of all dried films, up to at least $\sim 2/3$ rds peak fractional mass gain. Square-root-of-time dependence of mass gain could result from either Fickian diffusion of water into films or capillary pressure-driven flow of water through interconnected film pores. The former case is derived by solving the diffusion equation along the film thickness dimension, resulting in the following approximate solution at early immersion times^{38,39}:

$$\frac{M(t)}{M_\infty} = \frac{4}{\sqrt{\pi}} \frac{\sqrt{Dt}}{l}, \quad (1)$$

where t is time, $M(t)$ is fractional mass gain, D is molecular diffusivity of water, l is film thickness, and M_∞ is the fractional mass gain at saturation. M_∞ is also

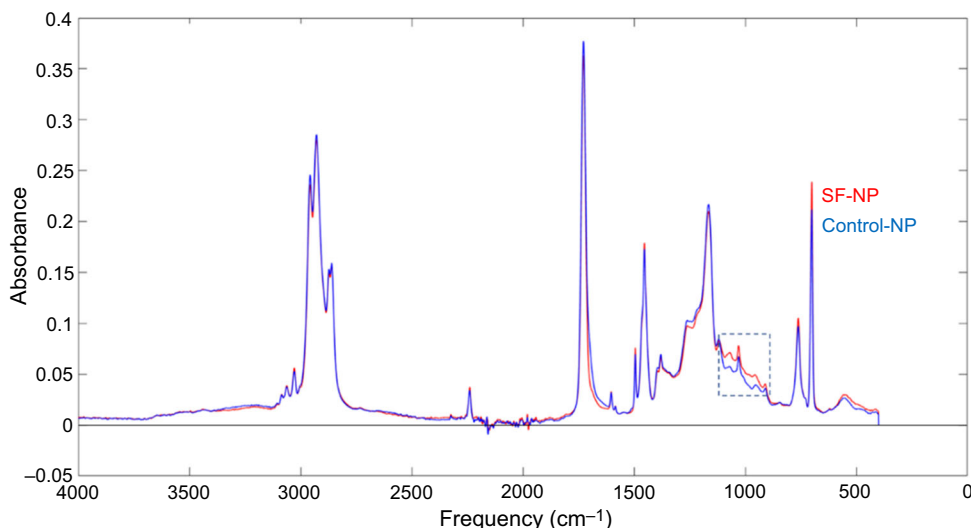


Fig. 3: ATR-FTIR results of free-standing control-NP and SF-NP films with absorbance on the y-axis and frequency on the x-axis, with significantly different infrared absorbances between 1100 and 900 cm⁻¹ frequencies

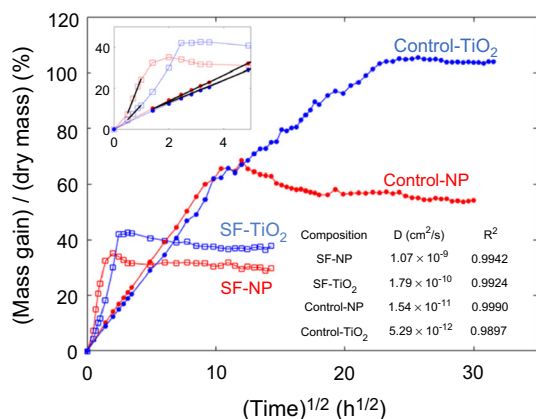


Fig. 4: Fractional mass gains of latex films immersed in DI water over time. Each data point is the average of values from 5 repeat samples. The inset more clearly displays water absorption behavior at short timescales along with the results of the linear fitting. Fit lines are truncated near the origin for greater clarity. The table displays water diffusivity and R² value obtained from fitting for each film composition

termed the water absorption capacity, and experimentally determined as peak fractional mass gain in Fig. 4.

The latter case is derived by assuming that water penetration through open dry pores is approximated as penetration through thin parallel tubes to arrive at the Washburn equation⁴⁰:

$$L(t) = \sqrt{\frac{\gamma r t \cos(\varphi)}{2\eta}}, \tag{2}$$

where $L(t)$ is the length of water penetration along tubes, $\gamma = 73.08$ mN/m is water surface tension,⁴¹ r is tube radius, φ is contact angle between water and latex

film, and $\eta = 1.002$ mPa s is bulk water viscosity.⁴² Assuming that $L(t) = 0$ when $M(t) = 0$, $L(t) = \frac{l}{2}$ when $M(t) = M_\infty$, and proportionality between $L(t)$ and $M(t)$, the Washburn equation relates fractional mass gain to time:

$$\frac{M(t)}{M_\infty} = \sqrt{\frac{\gamma r t \cos(\varphi)}{2\eta l^2}}. \tag{3}$$

Both equations (1) and (3) assume constant film thickness, which neglects the effect of volume expansion upon water absorption. Assuming that the partial molar volumes of absorbed water and bulk water are identical, the largest fraction volume increase at water absorption capacity—control-TiO₂ with dry density of 1.7 g/cm³ and 106 wt.% capacity—is 180%. This volume expansion corresponds to a fraction thickness increase of 41% as the films (unconstrained) are assumed to be isotropic. Note that in order to reduce anisotropy, the films used in this study are not constrained in-plane. They were formed on a non-stick substrate, and then peeled off prior to water immersion. Still, the dried film is probably not perfectly isotropic structurally, because of the evaporation direction during its formation, and therefore the isotropy is a model assumption. This assumption may not apply equally well to actual constrained films.

Since both D in equation (1) and r in equation (3) scale with l^2 when all other parameters are kept constant, a 41% increase in l results in a 99% increase in D and r . That is, l is 0–41% larger than assumed, and D and r are actually 0–99% larger than the values obtained from fitting experimental data. Since equation (3) assumes that r remains constant during the water absorption process whereas pore shape may change after water absorption, values of r obtained by

fitting equation (3) to experimental data represent the average tube radius during the water ingress process.

To assess the water permeation mechanism, equation (3) was fitted to experimental data in Fig. 4 to extract tube radius by linear fitting of $M(t)$ versus \sqrt{t} between 0 and 48 h for control-NP, 15–60 min for SF-NP, 0–192 h for control-TiO₂, and 15–60 min for SF-TiO₂. Estimating $\cos(\varphi) = 0.1$ (correct to within an order of magnitude⁴³) yields tube radii ranging from 2×10^{-16} m for control-TiO₂ to 5×10^{-14} m for SF-NP, many orders of magnitude lower than a typical atom diameter of 10^{-10} m, which is physically unrealistic. However, the viscosity of water with at least one dimension constrained to nanometer or sub-nanometer length scale may be 4–10 orders of magnitude larger than the viscosity of bulk water as measured experimentally.^{44–47} r is directly proportional to η at constant slope of $M(t)$ versus \sqrt{t} , so the lowest tube radius will be raised to $10^{-12} \sim 10^{-6}$ m—well within a physically realistic range—when confined water viscosity is assumed to be 4–10 orders of magnitudes larger than bulk. However, significant viscosity enhancement is reported only when the length scale of confinement is approximately 1 nm or smaller.^{46,47} Therefore, it is possible that permeation through pores with a radius of around 1 nm or smaller contributes to water entry into the latex films.

By applying results from the linear fitting of $M(t)$ versus \sqrt{t} to equation (1), water diffusivity values of 2×10^{-11} cm²/s for control-NP, 1×10^{-9} cm²/s for SF-NP, 5×10^{-12} cm²/s for control-TiO₂ and 2×10^{-10} cm²/s for SF-TiO₂ were obtained. Since the bulk polymer chemistries of control and SF latex particles are very similar, the factor-of-70 diffusivity difference between SF-NP and control-NP and factor-of-30 diffusivity difference between SF-TiO₂ and control-TiO₂ are most likely explained by different latex particle boundary compositions. While latex particle interdiffusion during film formation resulted in films with sufficient mechanical robustness to be peeled from release papers, it is proposed that interdiffusion was insufficient to result in roughly equal atomic density between latex particle boundaries and bulk. That is, latex particle boundaries are assumed to have a higher volume fraction of free volume compared to latex particle interiors, and the resulting higher diffusivity⁴⁸ at boundaries combined with these boundaries forming a percolating network through the film may cause boundaries to dominate the film's diffusivity. It is proposed that boundaries in SF polymer-containing film have higher local water absorption capacity compared to control polymer-containing film due to hydrophilic sulfoxide-rich SF groups at boundaries, which leads to higher measured diffusivities in SF polymer-containing films.⁴⁹ Water whitening⁵⁰ observed in control-NP and SF-NP films after DI water immersion further suggests that local levels of water absorption in the bulk latex particles and latex boundaries are different. The factor-of-3 diffusivity differ-

ence between control-NP and control-TiO₂ and the factor-of-6 diffusivity difference between SF-NP and SF-TiO₂ is not due to the blocking of water diffusion paths by TiO₂ particles. Since TiO₂ particles are randomly and mostly individually dispersed within both control-TiO₂ and SF-TiO₂ films as shown in Figs. 5a and 5b, they reduce water-accessible cross-section area and diffusivity by only 16% relative to NP films as TiO₂ fraction is controlled at 16 vol.% in formed pigmented films. Instead, reduced water diffusivity after TiO₂ addition may be attributed to TiO₂ dispersants which reduce diffusivity in the boundary network by forming stronger film-water bonds, and consequently raising the activation energy for water diffusion.⁴⁹ That is, water diffusion, partially through a percolating boundary network, is another plausible mechanism for water ingress into films.

Despite higher local water absorption at boundaries in SF polymer-containing films relative to control-polymer-containing films, SF polymer-containing films exhibit lower water absorption capacity as shown in Fig. 4. This apparent contradiction may be explained by the lower surfactant concentration in SF polymer-containing films due to the greater stability of latex particles with hydrophilic SF surface groups in dispersion, and the dominant effect of surfactant concentration on overall water absorption capacity.¹⁰

Effect of water absorption on ion leaching

To study ion transport, measurements of conductivity over time due to the leaching of latex film ions into DI water are shown in Fig. 6a. Versions of this figure with error bars are shown in Figs. S3 and S4. Conductivity rise is the complementary measurement to mass gain in Fig. 4: the former experiment measures ion transport out of films into DI water, while the latter measures water absorption into films. The conductivity rise rate in Fig. 6b is equal to the derivative of conductivity with respect to time. For SF-NP and SF-TiO₂, the derivative

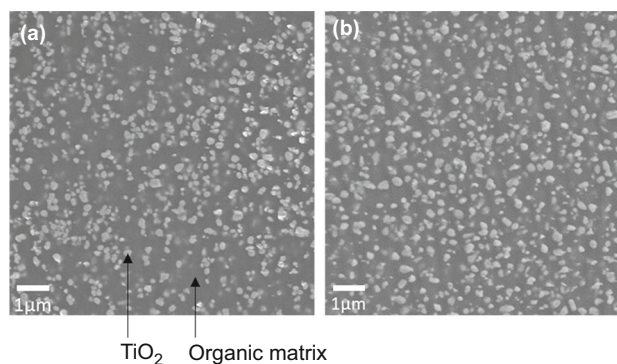


Fig. 5: (a) and (b) are ion-polished cross-section SEM images of control-TiO₂ and SF-TiO₂ films, respectively. The brightness of images was digitally adjusted to be comparable

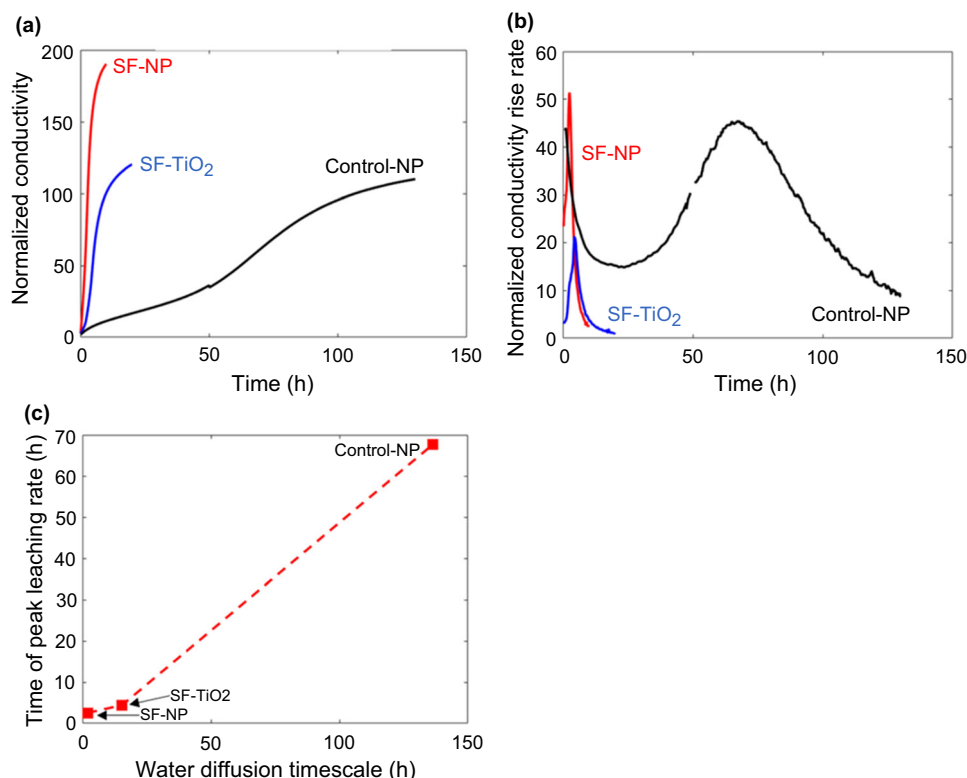


Fig. 6: (a) Conductivity versus immersion time of DI water baths into which latex films were placed. SF-NP and SF-TiO₂ data series are each averaged from five repeat samples at all times shown. Conductivities are normalized by DI water volume and latex film area, and consequently have units of ($\mu\text{S}/\text{cm}$) (mL/cm^2). (b) Conductivity rise rate versus immersion time, equal to the time derivative of data series shown in (a). Note that the conductivity rise rate of control-NP has been magnified by a factor of 30. Units of conductivity rise rate are ($\mu\text{S}/\text{cm}$) (mL/cm^2) ($1/\text{h}$). (c) Correlation between water diffusion timescale and time of peak ion leaching rate, extracted from (b) and Fig. 4, respectively

at some time is calculated by the slope of the best fit line through 7 points closest to that time, where data is assumed to be locally linear. For control-NP, the derivative is the slope through the closest 21 points. Despite averaging across multiple samples, significant noise in conductivity measurements appeared after 10, 20, and 60 h during SF-NP, SF-TiO₂, and control-NP leaching, respectively. This noise is attributed to the fractured film fragments, generated due to forces induced by stir bars, which temporarily lodge between electrodes in conductivity probes and thereby change the measured conductivity.

As shown in Fig. 6b, ion leaching conductivity rise rates of all films except control-TiO₂ (see Figs. S1 and S2) show a peak that precedes a final decrease over time. This behavior is contrary to that expected from Fickian diffusion of mobile ions out of films, which predicts that the rise rate should monotonically decrease over time due to depletion of mobile ion concentration, and hence mobile ion concentration gradient, within films. Figure 6c shows the correlation between water diffusion timescale and time at which rise rate peaks. The water diffusion timescale is defined as $t = l^2/4D$. Since water entry by diffusion and capillary flow have the same time-dependence, the

water diffusion timescale is a characteristic timescale for both mechanisms of water entry.

To demonstrate the coupled water and ion transport, the time of conductivity rise rate peak was shown to increase monotonically with increasing water diffusion timescale in Fig. 6c. It is proposed that this peak is due to the enhancement of mobile ion diffusivity by rising absorbed water concentration inside films. As the water concentration at mobile ion exit pathways progressively increases due to water absorption, the volume fraction of free volume increases at these pathways,⁵¹ leading to higher mobile ion diffusivity. Furthermore, the lack of a noticeable peak for control-TiO₂—which has the longest water diffusion timescale of all films—is because ion leaching had proceeded nearly to completion by the time water absorption had a significant impact on mobile ion diffusivity.

Semi-continuum model

A semi-continuum model was developed to explain the experimental results with coupled water absorption and ion transport. In this model, the film was modeled as a series of compartments stacked along the film's

thickness (see Fig. 7a) with water, mobile ions, and coalescent as the mobile species within an immobile matrix of polymer, pigment (if present), and other immobile species. To simplify the model, the mobile species are assumed to reside in a separate volume from the immobile species, which is defined as the hydrophilic volume. Since the model is coarse-grained, the compartment length scale is much larger than the latex particle diameter, so differences in concentration and transport rates between bulk latex particles and latex boundaries may be ignored. Indeed, since 80 compartments along the thickness of around 60 μm are used, the compartment length scale of 800 nm is much larger than the latex particle diameter of 100 nm.

The governing equations of the model are based on the proposed mechanisms from the experimental results. The first experimental conclusion is that water absorption may occur via both random-walk diffusion and pressure-driven flow. Generalizing this conclusion to all mobile species, it is proposed that transport may occur by a combination of diffusion and flow. Therefore, the following mass balance applies within each compartment:

$$\frac{d\hat{n}_{j,k}}{dt} = \hat{J}_{j,k-0.5} - \hat{J}_{j,k+0.5} + \hat{F}_{j,k-0.5} - \hat{F}_{j,k+0.5}. \quad (4)$$

Here, the indices j and k refer to the species (water w , mobile ions i or coalescent c) and the compartment number, respectively. \hat{J} is the Fickian diffusion flux and \hat{F} the convection-like elastic relaxation flux. For brevity, in parts of the subsequent derivation, we drop the index j , indicating that the expression is valid for all

species. A quantity with a half-integer compartment number is equal to the average of that quantity in the two nearest compartments. The present elastic compartment model assumes that all expansion due to water absorption is out-of-plane.

The diffusion flux is driven by the concentration gradient within the hydrophilic volume:

$$\begin{aligned} \hat{J}_{k+0.5} &= \frac{2D_{k+0.5}}{l_k + l_{k+1}} \epsilon_{k+0.5} \left[\frac{\hat{n}_k}{l_k \epsilon_k} - \frac{\hat{n}_{k+1}}{l_{k+1} \epsilon_{k+1}} \right] \\ &\approx \frac{2D_{k+0.5}}{l_k + l_{k+1}} \left[\frac{\hat{n}_k}{l_k} - \frac{\hat{n}_{k+1}}{l_{k+1}} \right]. \end{aligned} \quad (5)$$

Here, D is the diffusivity, l the length of the compartment, ϵ the hydrophilic volume fraction and \hat{n} the number of moles of species per unit area.

Absorption of water into a hydrophilic volume⁵² upon film immersion in water, which lowers the system's free energy, leads to elastic relaxation (see Fig. 7b) through an elastic relaxation flux:

$$\hat{F}_{k+0.5} = \hat{k}'_{k+0.5} [P_k - P_{k+1}]. \quad (6)$$

Here, \hat{k}' is a generic proportionality constant, and P_k is the pressure exerted on compartment k by the polymer matrix. In the present work, the pressure exerted by a fully relaxed film immersed in DI water is taken as the reference pressure. The pressure is evaluated from:

$$P_k = E \left[\frac{l_k}{l_k^0} - 1 \right]. \quad (7)$$

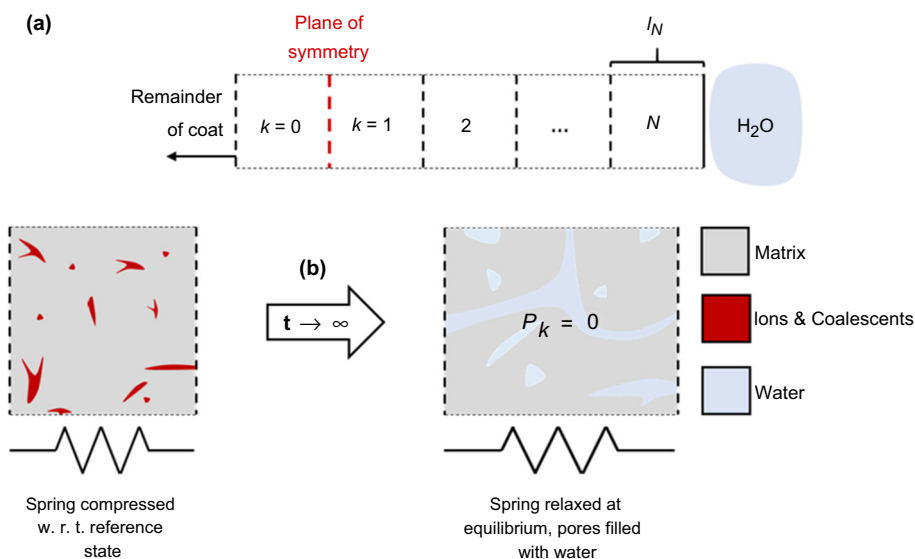


Fig. 7: (a) Schematic of the compartment model used in the present work. The film is assumed to be an infinite surface with a bisecting plane of symmetry. (b) At time $t = 0$, the film is visualized as a polymer matrix with mobile ions and coalescent inside the hydrophilic volume. At equilibrium, which is also the reference state, mobile ions and coalescent are fully removed; the hydrophilic volume is completely occupied by water. Relative to the reference state, the film is at elastic equilibrium, while initially, the film is under compression

Here, E is the Young's modulus of the matrix, and l^\ominus is the equilibrium length, defined as the length of a compartment when immersed for an infinitely long time in DI water. The derivation of the elastic relaxation flux is provided in the supplementary information, and the result is:

$$\hat{F}_k = \frac{2D_{k+0.5}}{l_k + l_{k+1}} \frac{\hat{V}_{k+0.5}}{R_g T} \frac{\hat{n}_{k+0.5}}{l_{k+0.5}} [P_k - P_{k+1}] \quad (8)$$

$$\hat{V}_k \approx \frac{\sum_j \hat{n}_{j,k} \hat{V}_j}{\sum_j \hat{n}_{j,k}} \quad (9)$$

Here, \hat{V}_j is the molar volume of species j , R_g the universal gas constant, and T the temperature.

In the expressions for diffusion flux (equation 5) and elastic relaxation flux (equation 6), the length of a compartment at any time is evaluated from the total amount of species within the compartment:

$$l_k = l_k(t=0) + \sum_j [\hat{n}_{j,k} - \hat{n}_{j,k}(t=0)] \hat{V}_j \quad (10)$$

The equilibrium length (l^\ominus) and the length associated with the matrix part of the film (l^{matrix}) is related by a stretch factor (λ_c):

$$l_k^\ominus = \lambda_c \left[l_k(t=0) - \sum_j \hat{n}_{j,k}(t=0) \hat{V}_j \right] \equiv \lambda_c l_k^{\text{matrix}} \quad (11)$$

The second experimental conclusion is that ion diffusivity is raised by increasing absorbed water concentration. It was assumed that the dependence of ion diffusivity on absorbed water concentration is described by percolation theory.⁵³ The simplest approximation of percolation theory is used:

$$D_{j,k} = \begin{cases} 0 & \text{if } \hat{n}_{w,k} < \hat{n}_{w,k}^\ominus \\ D_j^\ominus & \text{otherwise} \end{cases} \approx D_j^\ominus \frac{\exp\left[\frac{\hat{n}_{w,k} - \lambda_p \hat{n}_{w,k}^\ominus}{(1-\lambda_p) \hat{n}_{w,k}^\ominus / 5}\right]}{\exp\left[\frac{\hat{n}_{w,k} - \lambda_p \hat{n}_{w,k}^\ominus}{(1-\lambda_p) \hat{n}_{w,k}^\ominus / 5}\right] + \exp\left[-\frac{\hat{n}_{w,k} - \lambda_p \hat{n}_{w,k}^\ominus}{(1-\lambda_p) \hat{n}_{w,k}^\ominus / 5}\right]} \quad (12)$$

Here, D^\ominus is the diffusivity in the reference state; that is, trace amount of mobile ion/coalescent within a relaxed film immersed in DI water. $\hat{n}_{w,k}^\ominus$ is the equilibrium water content, which is evaluated by:

$$\hat{n}_{w,k}^\ominus = \frac{l_k^\ominus - l_k(t=0) + \sum_j \hat{n}_{j,k}(t=0) \hat{V}_j}{\hat{V}_w} \quad (13)$$

Initial and boundary conditions

Water is initially absent from the film:

$$\hat{n}_{w,k}(t=0) = 0 \quad (14)$$

Mobile ions and coalescent are initially uniformly distributed in the film:

$$\hat{n}_{j,k}(t=0) = \bar{C}_j l_k(t=0) \quad (15)$$

Here, \bar{C}_j is the initial bulk concentration of species j . Standard boundary conditions are used at the axis of symmetry and at the film/water interface and are listed in Table 1.

The hydrophilic volume fraction is equal to:

$$\epsilon_k = \sum_j \frac{\hat{n}_{j,k} \hat{V}_j}{l_k} \quad (16)$$

Model fitting procedure

The model is solved using 80 compartments in MATLAB and fitted to SF-NP and SF-TiO₂ experimental water absorption and ion transport data in Figs. 4 and 6a, respectively, using the in-built MATLAB genetic algorithm with command *ga*. Known and fitted parameters used in this process are listed in Table 2. The algorithm finds a set of fitted parameters that minimizes an objective function, which is proportional to the square of the difference between experimental data and the model prediction. The formula of the objective function and further details on the fitting procedure are provided in the supplementary information.

Table 1: List of boundary conditions at the plane of symmetry and at the film/water interface

At the plane of symmetry	At the film/water interface
$\hat{n}_{j,0} = \hat{n}_{j,1}$	$\hat{n}_{j,N+1} = 0$ for $j = i, c$
	$\epsilon_{N+1} = \epsilon_N$
	$l_{N+1} = l_N^\ominus$
	$\frac{l_{N+1} \epsilon_{N+1}}{\hat{V}_w} = \frac{1}{\hat{V}_w}$
	$P_{N+1} = 0$

The choice of l_{N+1} is arbitrary and has no impact on the simulation result. The boundary condition at the film/water interface is pure water in the hydrophilic volume of compartment $N+1$

Table 2: List of known and fitted parameter values for SF-NP and SF-TiO₂

	Description	Value		Unit
		SF-NP	SF-TiO ₂	
<i>Known parameters</i>				
l_T	Half-thickness of the film	29	32	μm
E	Young's modulus	0.1		GPa
A	Area of immersed film	29	33	cm ²
V_{bath}	Volume of DI water bath	77		cm ³
$m(t = 0)$	Dry film mass	216.1	334.6	mg
$\Sigma(t = 0)$	Initial DI water bath conductivity	0.597	0.928	μS/cm
\hat{V}_j	Molar volume	18 for water 14 for ions 210 for coalescents		mL/mol
$M_{r,j}$	Relative molecular mass	18 for water 29 for ions 190 for coalescents		g/mol
R_g	Universal gas constant	8.314		J/mol/K
T	Temperature	300		K
F	Faraday's constant	96,480		C/mol
$D_{i,\text{free}}$	Diffusivity of ionic species in DI water	1300		μm ² /s
z_i	Charge number of ionic species	1		
<i>Fitted parameters</i>				
λ_c	Equilibrium stretch factor for the polymeric part of the film	1.514	1.740	
D_w	Diffusivity of water in film	0.1486	0.1425	μm ² /s
D_i^\ominus	Diffusivity of ions in the reference state	0.1648	0.0615	μm ² /s
D_s^\ominus	Diffusivity of other soluble components in the reference state	0.0267	0.0107	μm ² /s
\bar{C}_i	Initial bulk concentration of ionic species	0.6559	0.4142	mol/L
\bar{C}_c	Initial bulk concentration of coalescent	0.3198	0.4278	mol/L

Film thickness, film area, DI water bath volume, dry film mass, and initial bath conductivity were measured experimentally. The Young's modulus is estimated from Hagan et al. (2009).⁵⁴ Ions are assumed to be composed of sodium chloride. Coalescents are assumed to be composed of di(propylene glycol) n-butyl ether, based on Fig. S6. The diffusivity of sodium chloride in water is estimated from Vitagliano and Lyons (1956).⁵⁵ The estimated parameters are expected to be accurate to within an order of magnitude

Model output and results

The film mass and solution conductivity are evaluated from the simulation output:

$$m = m(t = 0) + 2 \sum_j [m_j - m_j(t = 0)] \quad (17)$$

$$m_j = A \sum_k M_{r,j} \hat{n}_{j,k} \quad (18)$$

Here, m_j is the mass of species j , A is the area of the immersed film, and $M_{r,j}$ is the molecular mass of species j . The solution conductivity is evaluated from:

$$\Sigma = \Sigma(t = 0) + 2 \frac{z_i^2 D_{i,\text{free}} F^2 n_i(t = 0) - n_i}{R_g T V_{\text{bath}}} \quad (19)$$

$$n_i = A \sum_k M_{r,i} \hat{n}_{i,k} \quad (20)$$

Here, z_i is the charge number of the mobile ions, $D_{i,\text{free}}$ is the diffusivity of the mobile ions in DI water, F is Faraday's constant, and V_{bath} is the volume of the water bath.

Comparison of model and experiment

To gain a better physical understanding of the film system and the coupled water absorption and ion transport within it, the fitted results were superimposed on the data in Fig. 8. The model is able to capture the trends inherent in the data sets, especially the peak water absorption and non-Fickian ion leaching.

Peak water absorption arises due to the balance between diffusion and elastic relaxation fluxes. Initially, water is drawn into the film primarily by diffusion, leading to a rapid increase in film mass that scales linearly with \sqrt{t} . Diffusion flux into the film, proportional to osmotic pressure, as shown in equation (S2), decreases with increasing water absorption and loss of mobile ions and coalescent. Elastic relaxation

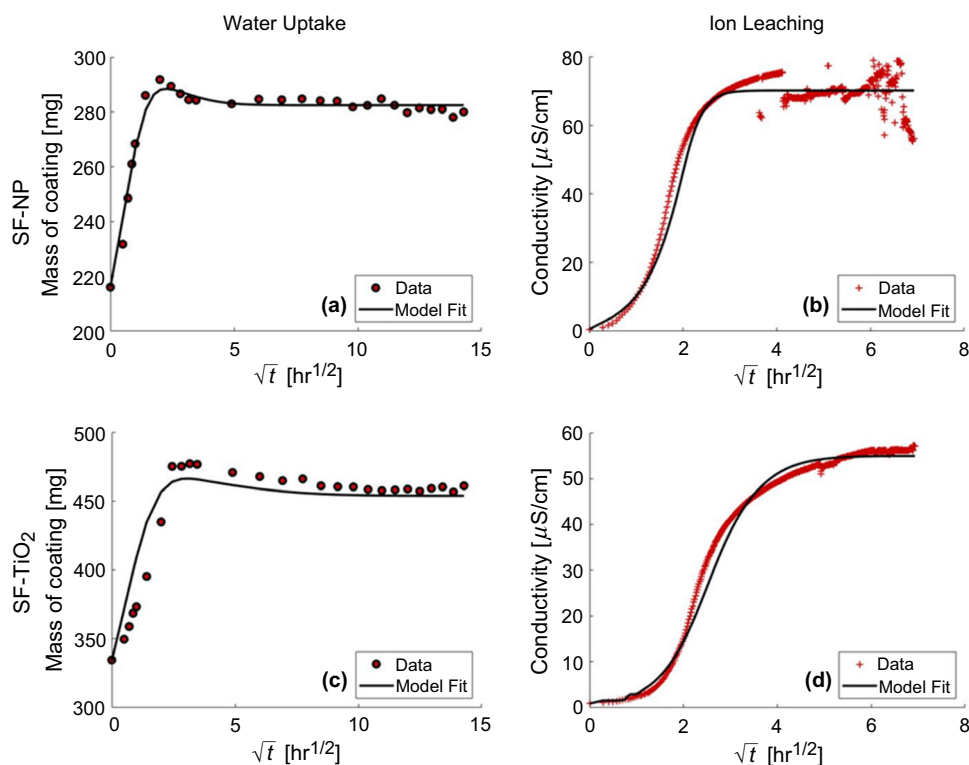


Fig. 8: Comparison between fitted results and experimental data for (a, b) SF-NP and (c, d) SF-TiO₂ using the water absorption data in Fig. 4 and the ion transport data in Fig. 6a. The fit is statistically significant at $p < 0.001$

flux out of the film, proportional to film thickness, increases with increasing water absorption. At the peak of water absorption, diffusion and elastic relaxation fluxes are approximately balanced, and beyond the peak, the dominance of elastic relaxation over diffusion results in a slow decrease in film mass. Osmotic pressure arises mostly due to the coalescent, which is an order of magnitude less mobile than water and mobile ions. As shown in Table 2, the diffusivity of water and mobile ions are within the same order of magnitude for both SF-NP and SF-TiO₂. The similarity in diffusivity implies that mobile ions do not contribute significantly to osmotic pressure, which requires much lower solute diffusivity compared to water diffusivity. In contrast, the diffusivity of coalescent is lower than that of water or mobile ions, allowing coalescent to contribute much more significantly to osmotic pressure.

As for the conductivity curve (Figs. 8b and 8d), its sigmoidal shape is counterintuitive based on the understanding of Fickian diffusion, which predicts a linear relationship between conductivity and \sqrt{t} . This effect is attributed to the delay associated with hydrophilic volume wetting and consequent diffusivity enhancement (see equation 12).

Though it predicts much of the transport behavior, the present model is not sufficient to fit the ion transport data of the control-NP film. This failure is probably due to the model's assumption of perfect

phase separation between polymer and absorbed water, whereas the spatial distribution of absorbed water is likely more homogeneous in reality. Experimental results suggest more spatially heterogeneous absorbed water distribution in SF polymer-containing films due to more hydrophilic boundaries, which explains the greater success of the model with these films.

Model validation

An additional mass balance closure experiment was performed to validate the model. Masses of 5 SF-TiO₂ film samples were measured immediately before immersion into separate DI water containers. Masses of all the samples were then measured again after 24 h DI water immersion, followed by 24 h drying in ambient conditions. Changes in the water bath conductivity of all samples after 24 h immersion were also measured. The immersion time period was chosen as 24 h because the film has approximately reached equilibrium in that time, as shown by the very small changes in water absorption and ion transport data in Figs. 4 and 6a, respectively, after 24 h.

Using these measured values, the masses of the mobile ions and the coalescent were calculated using sodium chloride and di(propylene glycol) n-butyl ether as the respective model components. The results of validation experiments are summarized in Table 3 and

Table 3: Validation data set is obtained by mass balance, assuming sodium chloride mobile ions and di(propylene glycol) n-butyl ether coalescent

	Experimental measurement	From Table 2
Mass of ions leached (mg)	2.19 ± 0.07	2.4
Mass of coalescents leached (mg)	16.8 ± 1.0	16.9

Considerable agreement is achieved despite the simplicity of the model

are in good agreement considering the simplicity of the model.

Further validations should be performed, in particular with regards to the stress applied by the polymer matrix on the hydrophilic volume (see equations 6 and 7) and the relationship between diffusion and flow conductance (see equation 19). These key assumptions could be investigated further using *in situ* synchrotron measurement, which allows real-time observation of polymer expansion and compartment size as a function of time. The resulting data set would provide a more convincing validation of the model, as opposed to the data set we have obtained, which is reliant on measurements averaged over the bulk of the coating.

Conclusions

The mutual influence and mechanisms of water absorption and ion transport in hydrated latex films are investigated using the *in situ* monitoring techniques of mass gain and conductivity rise upon immersion in DI water, respectively. Mutual influences are deduced by correlating water absorption and ion transport behavior of multiple film compositions. Water ingress into films proceeds either via capillary flow through pores or Fickian diffusion partially through a percolating boundary network. Absorbed water was found to enhance the diffusivity of mobile ions by raising the volume fraction of free volume in films. A semi-continuum model incorporating experimental conclusions is able to reliably fit the water absorption and ion transport data of SF-NP and SF-TiO₂ films. This model also explains the mass decrease after peak water absorption, as water diffusion flux into coating is less than the elastic relaxation flux out of the coating, leading to a net mass loss after the peak. These results have significant implications for future high-performance water-based anti-corrosion coating design. Higher water absorption capacity may lead to faster transport of ionic corrosive reactants, assuming these ion mobilities have the same dependence on absorbed water concentration as those in this study. Water absorption capacity, which may also affect delamination rate, may be lowered by stabilizing latex particles in dispersion using hydrophilic surface groups and consequently lowering the surfactant concentration within films.

Acknowledgments Funding for this project was supplied through a grant from Dow. We thank Drs. Paul Mwasame, Graham Abramo, Zhenwen Fu, and Thomas Kalantar from Dow for helpful discussions and suggestions. This work made use of the MRSEC Shared Experimental Facilities at MIT, supported by the National Science Foundation under Award Number DMR-1419807. This work was performed in part at the Center for Nanoscale Systems (CNS) of Harvard University, which is a member of the National Nanotechnology Coordinated Infrastructure Network (NNCI) supported by the National Science Foundation (NSF) under NSF Award No. ECCS-2025158.

Funding Open Access funding provided by the MIT Libraries.

Open Access This article is licensed under a Creative Commons Attribution 4.0 International License, which permits use, sharing, adaptation, distribution and reproduction in any medium or format, as long as you give appropriate credit to the original author(s) and the source, provide a link to the Creative Commons licence, and indicate if changes were made. The images or other third party material in this article are included in the article's Creative Commons licence, unless indicated otherwise in a credit line to the material. If material is not included in the article's Creative Commons licence and your intended use is not permitted by statutory regulation or exceeds the permitted use, you will need to obtain permission directly from the copyright holder. To view a copy of this licence, visit <http://creativecommons.org/licenses/by/4.0/>.

References

- Liu, Y, et al. "Source Profiles of Volatile Organic Compounds (VOCs) Measured in China: Part I." *Atmos. Environ.*, **42** 6247–6260 (2008)
- Steward, PA, Hearn, J, Wilkinson, MC, "An Overview of Polymer Latex Film Formation and Properties." *Adv. Colloid Interface Sci.*, **86** 195–267 (2000)
- Butler, LN, Fellows, CM, Gilbert, RG, "Effect of Surfactant Systems on the Water Sensitivity of Latex Films." *J. Appl. Polym. Sci.*, **92** 1813–1823 (2004)
- Gauthier, C, et al. "Reactive Surfactants in Heterophase Polymerization. XVII. Influence of the Surfactant on the

- Mechanical Properties and Hydration of the Films.” *J. Appl. Polym. Sci.*, **84** 1686–1700 (2002)
5. Li, J, et al. “Fabrication and Properties of Polysilsesquioxane-Based Trilayer Core-Shell Structure Latex Coatings with Fluorinated Polyacrylate and Silica Nanocomposite as the Shell Layer.” *J. Coat. Technol. Res.*, **15** 1077–1088 (2018)
 6. Šňupárek, J, Bidman, A, Hanuš, J, Hájková, B. “Water Absorption in Acrylic Latex Films.” *J. Appl. Polym. Sci.*, **28** 1421–1428 (1983)
 7. Teng, G, Soucek, MD, Yang, XF, Tallman, DE. “Effect of the Addition Mode of Cycloaliphatic Diepoxide on the Morphology and Film Properties of Crosslinkable Core-Shell Latex.” *J. Appl. Polym. Sci.*, **88** 245–257 (2003)
 8. Wu, S, Jorgensen, JD, Soucek, MD. “Synthesis of Model Acrylic Latexes for Crosslinking with Cycloaliphatic Diepoxides.” *Polymer (Guildf.)*, **41** 81–92 (2000)
 9. Xu, W, An, Q, Hao, L, Sun, Z, Zhao, W. “Synthesis and Properties of Cationic Fluorinated Polyacrylate Soap-Free Latex.” *J. Macromol. Sci. Part A Pure Appl. Chem.*, **50** 670–677 (2013)
 10. Chen, Y, Cheng, S, Wang, Y, Zhang, C. “Chemical Components and Properties of Core-Shell Acrylate Latex Containing Fluorine in the Shell and Their Films.” *J. Appl. Polym. Sci.*, **99** 107–114 (2006)
 11. Xu, W, et al. “Synthesis and Characterization of Novel Fluoroalkyl-Terminated Hyperbranched Polyurethane Latex.” *Appl. Surf. Sci.*, **436** 1104–1112 (2018)
 12. Wang, J, Zeng, XR, Li, HQ. “Preparation and Characterization of Soap-free Fluorine-Containing Acrylate Latex.” *J. Coat. Technol. Res.*, **7** 469–476 (2010)
 13. Yao, L, Yang, T, Cheng, S. “Synthesis and Characterization of Poly(fluorinated acrylate)/Silica Hybrid Nanocomposites.” *J. Appl. Polym. Sci.*, **115** 3500–3507 (2010)
 14. Li, Y, Zhu, J, Gao, X, Yu, Z. “Preparation and Properties of Phosphate-Fluorocarbon Acrylate Anticorrosion Emulsion.” *J. Macromol. Sci. Part A Pure Appl. Chem.*, **50** 248–254 (2013)
 15. Chen, S, Yan, W, Chen, L, Chen, Y, Xu, N. “Morphology and Microstructure of Core-Shell Hybrid Latexes Containing Fluoropolymer and Acrylic Copolymer.” *Colloid Polym. Sci.*, **284** 413–421 (2006)
 16. Li, G, Li, N, Wang, C, Niu, Y, Gong, X. “Synthesis and Properties of the Cationic Fluorocarbon Emulsifier-Free Latex in a New Micellar System.” *Colloid Polym. Sci.*, **292** 123–131 (2014)
 17. Lu, D, et al. “Role of Three Different Carboxylic Monomers in Acrylate Emulsion Copolymerization in the Presence of Reactive Emulsifier.” *J. Appl. Polym. Sci.*, **125** 2807–2813 (2012)
 18. Shui, X, Shen, Y, Fei, G, Wang, H, Zhu, K. “The Effect of Nonionic Monomer HAM on Properties of Cationic Surfactant-Free Acrylic/Alkyd Hybrid Emulsion.” *J. Appl. Polym. Sci.*, **132** 1–9 (2015)
 19. Ooi, SK, Cook, WD, Simon, GP, Such, CH. “Effects of Composition on the Water Uptake and Hydroplasticisation of the Glass Transition Temperature of Methacrylate Copolymers.” *Eur. Polym. J.*, **38** 903–910 (2002)
 20. Liu, D, Ichikawa, H, Cui, F, Fukumori, Y. “Short-Term Delayed-Release Microcapsules Spraycoated with Acrylic Terpolymers.” *Int. J. Pharm.*, **307** 300–307 (2006)
 21. Zhong, S, Sun, C, Gao, Y, Cui, X. “Preparation and Characterization of Polymer Electrolyte Membranes Based on Silicon-Containing Core-Shell Structured Nanocomposite Latex Particles.” *J. Power Sources*, **289** 34–40 (2015)
 22. Li, X, et al. “Synthesis and Characterization of Self-Crosslinked Polyurethane/ Polyacrylate Composite Emulsion Based on Carbonyl-Hydrazide Reaction.” *J. Polym. Res.*, **20** 1–9 (2013)
 23. Agarwal, N, Farris, RJ. “Water Absorption by Acrylic-Based Latex Blend Films and Its Effect on Their Properties.” *J. Appl. Polym. Sci.*, **72** 1407–1419 (1999)
 24. Luo, Z, Huang, H. “Glass-Transition Temperature of a Polyacrylate Latex Film and Its Water Whitening Resistance.” *J. Appl. Polym. Sci.*, **137** 1–8 (2020)
 25. Cui, M, Liu, C, Xu, Q, Li, R. “Effect of Hybrid Emulsifier (Reactive Coupling with Anionic) on the Properties of Acrylic Emulsion.” *J. Adhes. Sci. Technol.*, **29** 1758–1769 (2015)
 26. Martín-Fabiani, I, et al. “Enhanced Water Barrier Properties of Surfactant-Free Polymer Films Obtained by MacroRAFT-Mediated Emulsion Polymerization.” *ACS Appl. Mater. Interfaces*, **10** 11221–11232 (2018)
 27. Bilgin, S, Tomovska, R, Asua, JM. “Effect of Ionic Monomer Concentration on Latex and Film Properties for Surfactant-Free High Solids Content Polymer Dispersions.” *Eur. Polym. J.*, **93** 480–494 (2017)
 28. Ju, H, Sagle, AC, Freeman, BD, Mardel, JI, Hill, AJ. “Characterization of Sodium Chloride and Water Transport in Crosslinked Poly(ethylene oxide) Hydrogels.” *J. Memb. Sci.*, **358** 131–141 (2010)
 29. Peng, CC, Chauhan, A. “Ion Transport in Silicone Hydrogel Contact Lenses.” *J. Memb. Sci.*, **399–400** 95–105 (2012)
 30. Frankel, GS. “Pitting Corrosion of Metals: A Review of the Critical Factors.” *J. Electrochem. Soc.*, **145** 2186–2198 (1998)
 31. Song, Y, Jiang, G, Chen, Y, Zhao, P, Tian, Y. “Effects of Chloride Ions on Corrosion of Ductile Iron and Carbon Steel in Soil Environments.” *Sci. Rep.*, **7** 1–13 (2017)
 32. Dillon, JG, Schroeder, LW. “Permeability and Material Characteristics of Vulcanized Latex Film During and Following Cyclic Fatigue in a Saline Environment.” *J. Appl. Polym. Sci.*, **64** 553–566 (1997)
 33. An, D, Yang, L, Liu, B, Wang, TJ, Kan, C. “Diffusion Performance of Fertilizer Nutrient through Polymer Latex Film.” *J. Agric. Food Chem.*, **65** 10868–10874 (2017)
 34. Taylor, MA. “Synthesis of Polymer Dispersions.” In: Urban, D, Takamura, K (eds.) *Polymer Dispersions and Their Industrial Applications*, pp. 15–40. Wiley. <https://doi.org/10.1002/3527600582.ch2> (2002)
 35. Xu, GH, Dong, J, Severtson, SJ, Houtman, CJ, Gwin, LE. “Modifications of Surfactant Distributions and Surface Morphologies in Latex Films Due to Moisture Exposure.” *J. Phys. Chem. B*, **113** 10189–10195 (2009)
 36. Ziraldo, I, Watts, K, Luk, A, Lagalante, AF, Wolbers, RC. “The Influence of Temperature and Humidity on Swelling and Surfactant Migration in Acrylic Emulsion Paint Films.” *Stud. Conserv.*, **61** 209–221 (2016)
 37. Callister, WD. *Materials Science and Engineering*. Wiley, Berlin (2007)
 38. Amalvy, JI, Unzué, MJ, Schoonbrood, HAS, Asua, JM. “Reactive Surfactants in Heterophase Polymerization: Colloidal Properties, Film-Water Absorption, and Surfactant Exudation.” *J. Polym. Sci. Part A Pure Appl. Chem.*, **40** 2994–3000 (2002)
 39. Gatos, KG, Martínez Alcázar, JG, Psarras, GC, Thomann, R, Karger-Kocsis, J. “Polyurethane Latex/Water Dispersible Boehmite Alumina Nanocomposites: Thermal, Mechanical and Dielectrical Properties.” *Compos. Sci. Technol.*, **67** 157–167 (2007)
 40. Washburn, EW. “The Dynamics of Capillary Flow.” *Phys. Rev.*, **18** 206–209 (1921)
 41. Gittens, GJ. “Variation of Surface Tension of Water with Temperature.” *J. Colloid Interface Sci.*, **30** 406–412 (1969)

42. Korson, L, Drost-Hansen, W, Millero, FJ, “Viscosity of Water at Various Temperatures.” *J. Phys. Chem.*, **73** 34–39 (1969)
43. Tokuda, K, Ogino, T, Kotera, M, Nishino, T, “Simple Method for Lowering Poly (Methyl Methacrylate) Surface Energy with Fluorination.” *Polym. J.*, **47** 66–70 (2015)
44. Zhu, Y, Granick, S, “Viscosity of Interfacial Water.” *Phys. Rev. Lett.*, **87** 1–4 (2001)
45. Ortiz-Young, D, Chiu, HC, Kim, S, Voitchovsky, K, Riedo, E, “The Interplay Between Apparent Viscosity and Wettability in Nanoconfined Water.” *Nat. Commun.*, **4** 1–6 (2013)
46. Goertz, MP, Houston, JE, Zhu, XY, “Hydrophilicity and the Viscosity of Interfacial Water.” *Langmuir*, **23** 5491–5497 (2007)
47. Li, T, De, Gao, J, Szoszkiewicz, R, Landman, U, Riedo, E, “Structured and Viscous Water in Subnanometer Gaps.” *Phys. Rev. B Condens. Matter Mater. Phys.*, **75** 1–6 (2007)
48. Cohen, MH, Turnbull, D, “Molecular Transport in Liquids and Glasses.” *J. Chem. Phys.*, **31** 1164–1169 (1959)
49. Yasuda, H, Lamaze, CE, Peterlin, A, “Diffusive and Hydraulic Permeabilities of Water in Water-Swollen Polymer Membranes.” *J. Polym. Sci. Part A-2*, **9** 1117–1131 (1971)
50. Liu, Y, et al. “Explanations for Water Whitening in Secondary Dispersion and Emulsion Polymer Films.” *J. Polym. Sci. Part B Polym. Phys.*, **54** 1658–1674 (2016)
51. Yasuda, H, Lamaze, CE, Ikenberry, LD, “Permeability of Solutes Through Hydrated Polymer Membranes.” *Die Makromol. Chemie*, **118** 19–35 (1968)
52. Doi, M, *Soft Matter Physics*. Oxford University Press (2013)
53. Sahini, M, Sahimi, M, *Applications of Percolation Theory*. CRC Press (2003)
54. Hagan, EWS, Charalambides, MN, Young, CT, Learner, TJS, Hackney, S, “Tensile Properties of Latex Paint Films with TiO₂ Pigment.” *Mech. Time-Dependent Mater.*, **13** 149–161 (2009)
55. Vitagliano, V, Lyons, PA, “Diffusion Coefficients for Aqueous Solutions of Sodium Chloride and Barium Chloride.” *J. Am. Chem. Soc.*, **78** 1549–1552 (1956)
56. Cai, J, Perfect, E, Cheng, C, Hu, X, “Generalized Modeling of Spontaneous Imbibition Based on Hagen – Poiseuille Flow in Tortuous Capillaries with Variably Shaped Apertures.” *Langmuir*, **30** 5142–5151 (2014)
57. Van der Meer-Lerk, LA, Heertjes, PM, “The Influence of Pressure on Blister Growth.” *J. Oil Colour Chem. Assoc.*, **64** 30–38 (1981)
58. Lewis, GN, “The Osmotic Pressure of Concentrated Solutions, and the Laws of the Perfect Solution.” *J. Am. Chem. Soc.*, **30** 668–683 (1908)

Publisher’s Note Springer Nature remains neutral with regard to jurisdictional claims in published maps and institutional affiliations.